research papers

Engineering the band gap and optical properties of a two-dimensional molybdenum carbon fluoride MXene

Doan Thi Kieu Anh,[a] Luong Viet Mui,[b,c]* Pham Hong Minh,[a,b] Nguyen Thanh Binh[a] and Marilou Cadatal-Raduban[d,e]*

[a]Institute of Physics, Vietnam Academy of Science and Technology, 10 Dao Tan, Ba Dinh, Hanoi, Vietnam, [b]Osaka University ASEAN Campus Vietnam, 18 Hoang Quoc Viet, Cau Giay, Hanoi, Vietnam, [c]Graduate School of Engineering, Osaka University, 2-1 Yamadaoka, Suita, Osaka 565-0871, Japan, [d]Centre for Theoretical Chemistry and Physics, School of Natural Sciences, Massey University, Auckland 0632, New Zealand, and [e]Institute of Laser Engineering, Osaka University, 2-6 Yamadaoka, Suita, Osaka 565-0871, Japan. *Correspondence e-mail: luong-vm.eng@osaka-u.ac.jp, m.raduban@massey.ac.nz

Using first-principles density functional theory, we investigated the electronic and optical properties of monolayer and multilayer nanosheets of molybdenum carbon fluoride (Mo_2CF_2), a two-dimensional (2D) transition-metal carbide MXene. The indirect band gap of the Mo_2CF_2 semiconductor can be engineered by controlling the number of layers where the band gap energy changes from 0.278 eV for the monolayer to 0.249 eV for the trilayer nanosheet. The decrease in band gap energy in the multilayer is due to interlayer coupling, which splits the bands according to the number of layers. Mo_2CF_2 behaves as a metal with an anomalous dispersion and high optical conductivity at incident photon energies of 0.68–2.19, 3.49–6.68 and 7.30–8.31 eV. It has a relatively low reflectivity and is absorbing over a broad range of photon energies from about 0.429 (2890), 0.387 (3204) and 0.345 eV (3594 nm) for the monolayer, bilayer and trilayer nanosheets, respectively, achieving peak absorption in the vacuum ultraviolet region at about 7.9 eV (157 nm). The optical properties of Mo_2CF_2 can likewise be tuned by varying the number of layers. The unique behavior of its optical properties along with the ability to control its electronic and optical properties enhances the potential of 2D Mo_2CF_2 for various applications in the fields of electronics and energy storage.

1. Introduction

Since the discovery of graphene and its wonderful properties (Kaushik *et al.*, 2019; Ostovari *et al.*, 2018), two-dimensional (2D) materials with their extraordinary electronic, mechanical and optical properties (Georgiou *et al.*, 2012; Tamleh *et al.*, 2018) have attracted much research interest in the field of materials science. The recent discovery of a novel family of compounds called 2D transition-metal carbides, nitrides and carbonitrides (MXene) has gained significant attention from the scientific community and has spurred new interest in 2D materials (Khazaei *et al.*, 2019; Bae *et al.*, 2021; Naguib *et al.*, 2013; Anasori *et al.*, 2015). MXene has a general formula of $M_{n+1}X_nT_x$ ($n = 1$–3), where M indicates early transition metals (*e.g.* Sc, Ti, V, Nb, Mo, *etc.*), X stands for C and/or N, and T_x represents functional groups on the surface of the MXene, such as –OH, –O or –F (Naguib *et al.*, 2011; Hong *et al.*, 2020; Champagne *et al.*, 2018). MXenes have a huge potential in a wide range of applications, such as energy storage (Yorulmaz *et al.*, 2016; Anasori *et al.*, 2017), sensing (Sinha *et al.*, 2018; Khazaei *et al.*, 2012), catalysis (Peng *et al.*, 2018; Wang *et al.*, 2018; Li & Wu, 2019) and the development of electronic devices (Zhang & Nicolosi, 2019).
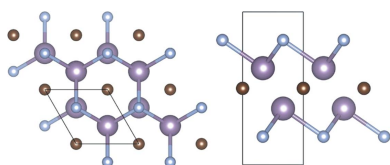
Table 1
Calculated band gap energy, unit-cell parameters and bond lengths for the bulk and two-dimensional layered Mo_2CF_2.

	Band gap energy (eV)	$a = b$ (Å)	c (Å)	d_{Mo-C} (Å)	d_{Mo-F} (Å)
Bulk	0.237	3.2738	6.7495	2.1125	2.2960
Trilayer	0.249	3.2798	35.7058	2.1154	2.3036
Bilayer	0.258	3.2793	35.7128	2.1151	2.3032
Monolayer	0.278	3.2786	35.7215	2.1148	2.3029

Molybdenum carbon fluoride (Mo_2CF_2) is a MXene consisting of the molybdenum (Mo) transition metal, carbon (C) and functionalized by fluorine (F). Khazaei *et al.* (2014) reported that a monolayer Mo_2CF_2 is an indirect band gap semiconductor with a narrow band gap of 0.27 eV and the most stable Mo_2CF_2 (hollow site–hollow site) structure is a promising thermoelectric material. Monolayer Mo_2CF_2 has many excellent properties, such as high capacity, outstanding mechanical strength and good flexibility. Therefore, this material has a great potential as an anode material for Li-ion batteries, as well as in various applications, including electronics and energy storage (Mehta *et al.*, 2019).

Despite previous works on several MXenes, including $Ti_3C_2T_2$, $Nb_4C_3T_x$ and V_2C- , with a wide variety of applications (Khazaei *et al.*, 2019; Bae *et al.*, 2021; Champagne *et al.*, 2018; Mostafaei & Abbasnejad, 2021; Khan *et al.*, 2019), research on the electronic and optical properties of Mo_2CF_2, and how the number of layers affects these properties is still lacking. The ability to control the band gap of a material is very important for its application in the field of electronic devices. As a material with exciting prospects for electronics and energy storage applications, the ability to control the electronic structure and hence the band gap of Mo_2CF_2 will

greatly enhance its potential. However, the ability to control the band gap of Mo_2CF_2 has not yet been demonstrated. Therefore, this work investigates the structural, electronic and optical properties of monolayer, bilayer and trilayer nanosheets of Mo_2CF_2 (collectively referred to as 2D layered Mo_2CF_2) using first-principles calculations in the framework of the generalized gradient approximation (GGA) implemented by the Perdew–Burke–Ernzerhof (PBE) functional. Our results illustrate how the electronic structure, band gap energy and optical properties can be controlled by manipulating the number of layers in a 2D Mo_2CF_2.

2. Computational method

The crystal structures of the bulk and 2D layered Mo_2CF_2 were visualized using *VESTA* (Momma & Izumi, 2011). The top and side views of bulk Mo_2CF_2 are shown in Figs. 1(*a*) and 1(*b*). Bulk Mo_2CF_2 consists of a layer of C atoms sandwiched between Mo atoms and two layers of Mo atoms halogenated by F atomic layers on each side. It has a hexagonal structure and space group $P6_3/mmc$ (No. 194). The side view of the relaxed configurations of the monolayer, bilayer and trilayer nanosheet is illustrated in Fig. 1. The atomic coordinates used to construct and visualize the bulk structure are Mo1 (0.333, 0.667, 0.368), Mo2 (0.667, 0.333, 0.632), C (0.000, 0.000, 0.500), F1 (0.667, 0.333, 0.184) and F2 (0.333, 0.667, 0.8156). The atomic coordinates (Wyckoff positions) and unit-cell parameters are taken from a previous report (Khazaei *et al.*, 2014) and were optimized using the GGA–PBE functional with the convergence criterion of 510^{-6} eV per atom. The Mo—C and Mo—F bonds are strong, with mixed covalent, metallic and ionic characteristics. On the other hand, the F—F bonds are weaker and more reactive, allowing a monolayer to be easily exfoliated from the bulk (Zhu *et al.*, 2017). The structure of the monolayer was constructed in *VESTA* starting from the 111 unit cell of the bulk crystal and making the value of the *c* axis five times greater than that of the bulk, thereby obtaining a 115 supercell. The number of layers was increased by adding a layer into the unit cell while keeping the lattice parameter along the *c* axis fixed. The structure from monolayer to multilayer is optimized every time a layer is added. The optimized unit-cell parameters are shown in Table 1.

The electronic band structures of bulk and 2D layered Mo_2CF_2 were calculated based on density functional theory (DFT) within the generalized gradient approximation (GGA) using the Perdew–Burke–Ernzerhof (PBE) functional. The calculations were implemented in the CASTEP code (Segall *et al.*, 2002; Accelrys, 2010) with a sufficiently high plane-wave basis cut-off of 500 eV. In all calculations, a 551 Monkhorst–Pack *k*-point grid was used to generate the initial charge density.

The optical properties of the bulk and 2D layered Mo_2CF_2 were extracted from the frequency-dependent complex dielectric function after applying a scissors correction to account for the excited-state nature of the optical properties. The complex dielectric function represents the linear response of
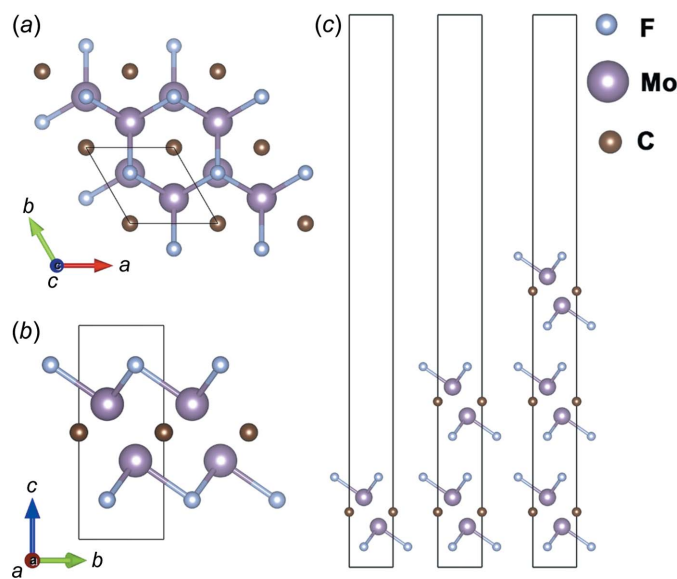

Figure 1
The crystal structures of Mo_2CF_2 showing (*a*) a top view and (*b*) a side view of bulk Mo_2CF_2, and (*c*) a side view of the monolayer (left), bilayer (middle) and trilayer (right) nanosheets of Mo_2CF_2.

the system to an external electromagnetic field and consists of a real and imaginary part as follows:

$$\varepsilon(\omega) = \varepsilon_1(\omega) + i\varepsilon_2(\omega), \qquad (1)$$

where ω is the optical frequency and $\varepsilon_1(\omega)$ and $\varepsilon_2(\omega)$ are the real and imaginary parts of the dielectric function, respectively. The real part $\varepsilon_1(\omega)$ of the dielectric function can be obtained from the imaginary part $\varepsilon_2(\omega)$ using the Kramers–Kronig relationships (Hutchings *et al.*, 1992; Kronig, 1926; Kramers, 1927).

$$\varepsilon_1(\omega) = 1 + \frac{2}{\pi} P \int_0^\infty \frac{\omega' \varepsilon_2(\omega')}{\omega'^2 - \omega^2 + i\eta} d\omega', \qquad (2)$$

where P is the principal value, η is an infinitesimal complex shift with a value of 0.1 and ω is the frequency over which the equation is being integrated. From the frequency-dependent complex dielectric function, other optical parameters, such as the absorption coefficient $\alpha(\omega)$, refractive index $n(\omega)$, reflectivity $R(\omega)$ (Qiu *et al.*, 2018) and conductivity (σ) (Accelrys, 2010), were calculated using the following equations, where c is the speed of light:

$$\alpha(\omega) = \sqrt{2} \frac{\omega}{c} \left[\sqrt{\varepsilon_1^2(\omega) + \varepsilon_2^2(\omega)} - \varepsilon_1(\omega) \right]^{1/2} \qquad (3)$$

$$n(\omega) = \frac{1}{\sqrt{2}} \left[\sqrt{\varepsilon_1^2(\omega) + \varepsilon_2^2(\omega)} - \varepsilon_1(\omega) \right]^{1/2} \qquad (4)$$

$$R(\omega) = \left\| \frac{\sqrt{\varepsilon_1(\omega) + i\varepsilon_2(\omega)} - 1}{\sqrt{\varepsilon_1(\omega) + i\varepsilon_2(\omega)} + 1} \right\|^2 \qquad (5)$$

$$\sigma(\omega) = \frac{\omega \varepsilon_2}{4\pi} - \frac{i\omega(\varepsilon_1 - 1)}{4\pi} \qquad (6)$$

3. Results and discussion

3.1. Crystal structure and electronic band structure

The unit-cell parameters and bond lengths for the bulk and 2D layered Mo_2CF_2 are summarized in Table 1. Our result for the monolayer is in good agreement with previous reports that numerically calculated the electronic structure of monolayer Mo_2CF_2 (Khazaei *et al.*, 2014). Experimental results for the band gap energy, unit-cell parameters, and bond lengths of bulk and 2D layered Mo_2CF_2 are still lacking.

Figs. 2(*a*)–2(*d*) show the electronic band structures of bulk and 2D layered Mo_2CF_2 calculated along the high-symmetry
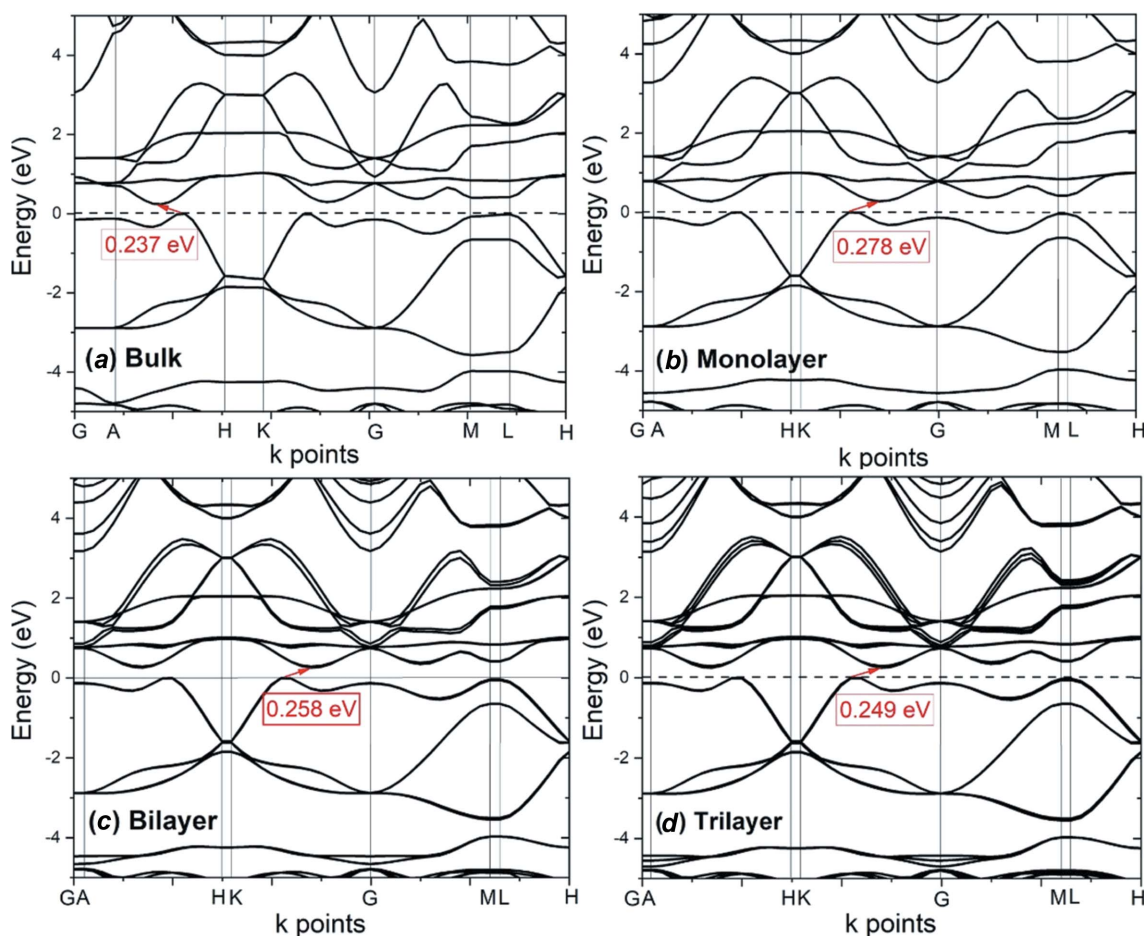

Figure 2
Electronic band structures of (*a*) bulk, (*b*) monolayer, (*c*) bilayer and (*d*) trilayer Mo_2CF_2

k-points path *G–A–H–K–G–M–L–H* in the first Brillouin zone. In these figures, the valence band maxima are shifted to zero energy. The band structures exhibit similar band shapes, particularly for the valence and conduction bands. All the materials are seen to be indirect band gap semiconductors. The maximum of the valence band and the minimum of the conduction band of the monolayer and multilayer are located at the *k*-point between *G* and *K*, while the bulk has the band gap located at the *k*-point between *H* and *A*.

The band gap energies of the monolayer, bilayer, trilayer and bulk Mo_2CF_2 are 0.278, 0.258, 0.249 and 0.237 eV, respectively, as summarized in Table 1. The 0.278 eV band gap energy obtained from our calculations for the monolayer is in good agreement with the previously reported band gap energy of 0.27 eV calculated using GGA–PBE (Khazaei *et al.*, 2014). In general, the band gap energy decreases as the number of layers is increased. The decrease in band gap energy can be attributed to interlayer coupling, which results in the splitting of the bands. As can be seen in Figs. 2(*b*) (monolayer), 2(*c*) (bilayer) and 2(*d*) (trilayer), band splitting increases progressively from the monolayer to the trilayer, and the splitting depends on the number of layers. As the number of layers increases, the splitting of bands due to the stronger interlayer coupling results in a decrease in the band gap

energy. In comparison, band splitting in the bulk Mo_2CF_2 is relatively small, which indicates that the couplings in the bulk are weak van der Waals interactions. These results indicate that the band gap of 2D layered Mo_2CF_2 could be engineered by controlling the number of layers. The ability to manipulate the band gap energy makes Mo_2CF_2 a promising material for applications in the field of electronic devices.

The total and partial density of states for the bulk and 2D layered Mo_2CF_2 are shown in Fig. 3. The valence band maximum and conduction band minimum are mainly composed of Mo-*d* states with a small overlap with C-*p* and F-*p* states. The Mo-*d* states also play a dominant role in the conduction band above the Fermi level, which confirms the partially occupied Mo^{2+} $4d^2$ orbital.

3.2. Optical properties

Fig. 4(*a*) shows the real part of the dielectric function, $\varepsilon_1(\omega)$, for the bulk and 2D layered Mo_2CF_2. The calculated values of $\varepsilon_1(0)$ are 5.76, 10.58 and 1.42 eV for the monolayer, bilayer and trilayer Mo_2CF_2, respectively. From 0 to 6 eV, the intensity of the peaks is seen to increase as the number of layers increases. The maximum value for $\varepsilon_1(\omega)$ is achieved at around 0.67 eV for all the materials. The higher value of $\varepsilon_1(\omega)$ shows a
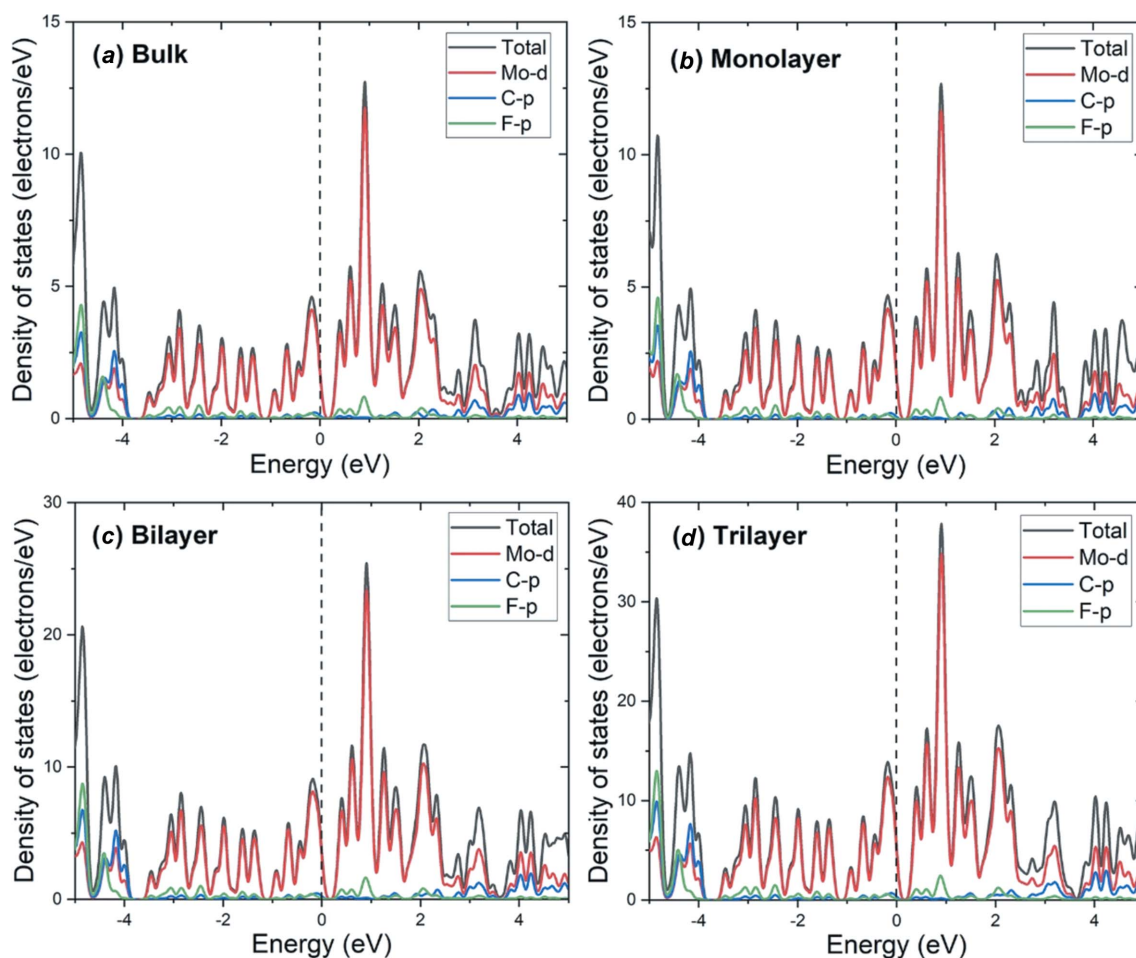

Figure 3
Total and partial density of states for (*a*) bulk, (*b*) monolayer, (*c*) bilayer and (*d*) trilayer Mo_2CF_2. The dashed lines represent the Fermi level.

greater ability for the polarization of low incident photon energy as the number of layers increases. Moving towards higher incident photon energy, an inflection point is observed around 6 eV, where $\varepsilon_1(\omega)$ takes on negative values. Above 6 eV, the intensity of the peaks appears to decrease (becomes more negative) as the number of layers increases. In the photon energy intervals 0.68–2.19, 3.49–6.68 and 7.30–8.31 eV, the bulk and 2D layered Mo_2CF_2 behave as a metal owing to anomalous dispersion. Dispersion is the property of materials whereby the refractive index changes as a function of wavelength. In normal dispersion, the refractive index increases as the photon energy increases (wavelength decreases), meaning that longer wavelengths are bent less compared to shorter wavelengths. The anomalous dispersion is confirmed by the plot of the refractive index as a function of photon energy [Fig. 4(b)]. Here, the refractive index decreases as the photon energy increases in the photon energy intervals 0.76–2.41, 3.66–6.89 and 7.43–8.94 eV. In normal dispersion, the refractive index should increase as the photon energy increases, as observed in the ranges 0–0.76, 2.41–3.66 and 6.89–7.43 eV. It is also interesting to note that when the incident photon energy is greater than 8.52 eV, the value of the refractive index is less than one, which is characteristic of metals. Comparing the
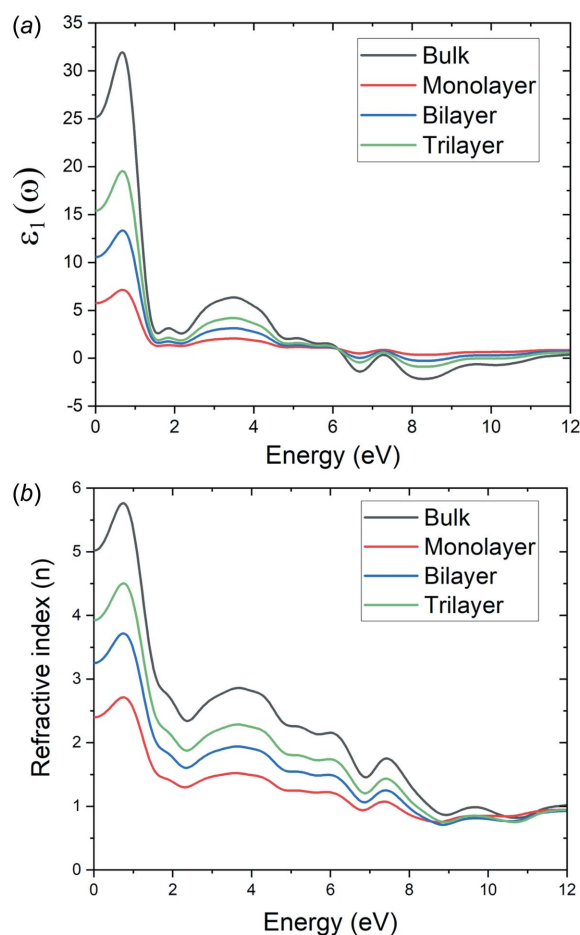
refractive index values of the 2D layered Mo_2CF_2, the refractive index can be increased by increasing the number of layers. These results suggest that the static dielectric constant and the optical dispersion characteristics of the 2D layered Mo_2CF_2 can also be manipulated by controlling the number of layers.

The imaginary part of the dielectric function, $\varepsilon_2(\omega)$, is shown in Fig. 5(a). This component is related to the transitions between the valence and conduction bands, and therefore to the electronic structure of Mo_2CF_2 and the absorption of the incident photons. The optical band gaps of the bulk and 2D layered Mo_2CF_2 can then be estimated from $\varepsilon_2(\omega)$ and these are 0.220, 0.178 and 0.136 eV for the monolayer, bilayer and trilayer Mo_2CF_2, respectively. These optical band gap energies are smaller than the electronic band gap energies obtained from the electronic structures (and summarized in Table 1). The discrepancy comes from the Coulombic interaction between electrons in the conduction band and holes in the valence band, as well as the exclusion of excitonic effects in the approximation (Cadatal-Raduban et al., 2020). Nevertheless, a similar trend to the electronic band gap energy is observed, wherein the optical band gap decreased as the number of layers increased. Above the optical band gap energy, a sharp rise in the intensity of $\varepsilon_2(\omega)$ is observed, with its peak appearing at 1.12 eV for all the materials. The peak corresponds to the electron transitions between the Mo-4d states to the Mo-5d states, as indicated by the density of states of Mo_2CF_2 (Fig. 3). The absorption coefficient and extinction coefficient of bulk and 2D layered Mo_2CF_2 is shown in Figs. 5(b) and 5(c), respectively. Regardless of the number of layers, Mo_2CF_2 is seen to be absorbing over a broad range of photon energies up to the vacuum ultraviolet region (greater than 6 eV photon energy or less than 200 nm wavelength), with a lower photon energy cut-off of 0.429, 0.387 and 0.345 eV for the monolayer, bilayer and trilayer nanosheets, respectively, which is in the mid-infrared wavelength region (wavelengths of about 2890, 3204 and 3594 nm for the monolayer, bilayer and trilayer nanosheets, respectively). Its peak absorption range is in the vacuum ultraviolet region from about 6 to 11 eV (wavelengths of about 207 to 112 nm), with an absorption peak at around 7.9 eV (157 nm). The extinction coefficient measures the loss of photon energy due to absorption and scattering, and therefore mimics the trend of $\varepsilon_2(\omega)$. Like the trend observed for $\varepsilon_2(\omega)$, where the intensity of $\varepsilon_2(\omega)$ increased as the number of layers increased, the value of the absorption and extinction coefficients also increased as a function of the number of layers. This indicates that the absorption of Mo_2CF_2 can also be manipulated by varying the number of layers.

Fig. 6 shows the reflectivity of bulk and 2D layered Mo_2CF_2. The reflectivity of the bilayer and trilayer Mo_2CF_2 are 0.28 and 0.35 at 0 eV, which means that about 28 and 35% of the incident light is reflected. A relatively low reflectivity is observed as the incident photon energy increases. In general, the reflectivity has a decreasing trend at photon energies between about 5 and 12 eV (about 248 and 103 nm). As reflectivity defines the ability of a material to reflect the
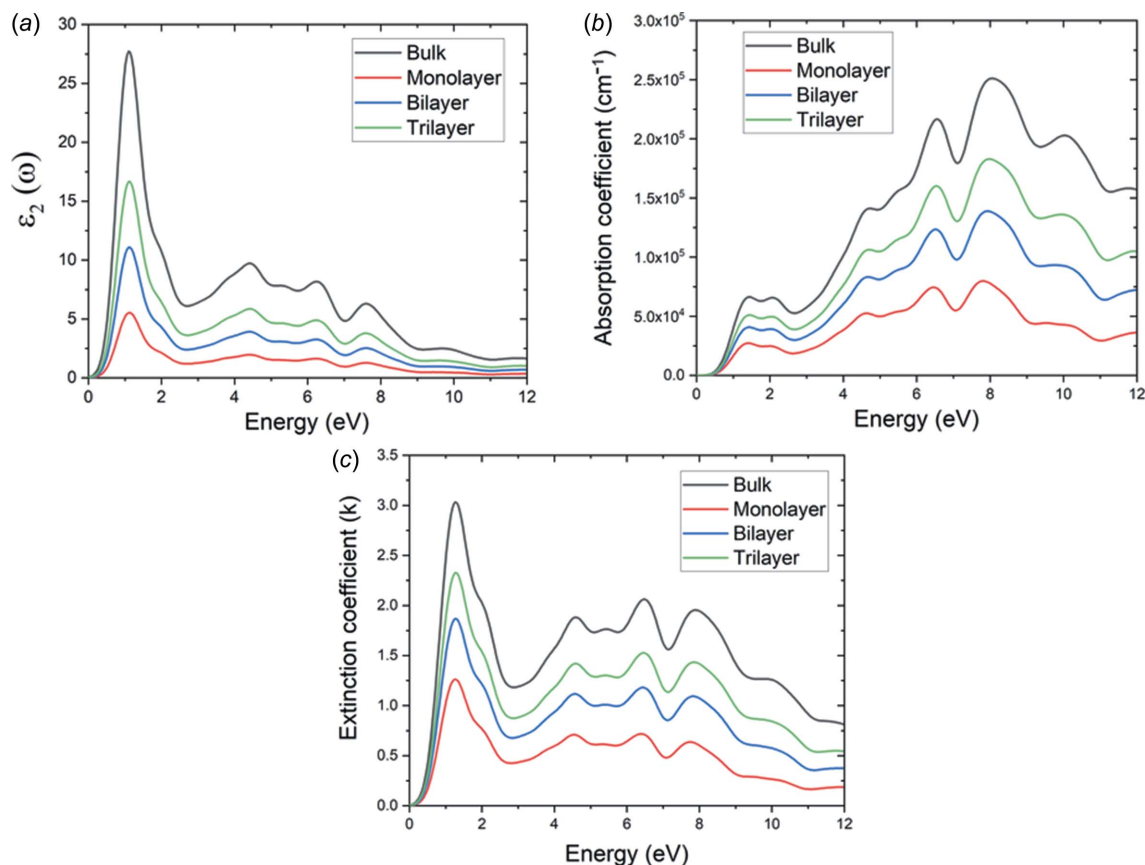

Figure 4
(a) Real part of the dielectric function [$\varepsilon_1(\omega)$] and (b) refractive index (n) as a function of incident photon energy for bulk and 2D layered Mo_2CF_2.

Figure 5
(a) Imaginary part of the dielectric function $[\varepsilon_2(\omega)]$, (b) absorption coefficient and (c) extinction coefficient (k) as a function of incident photon energy for bulk and 2D layered Mo_2CF_2.

incident photons, Mo_2CF_2 could be suitable as an antireflective coating, especially in the vacuum ultraviolet wavelength region. Furthermore, for this purpose, a smaller number of layers appears to be more advantageous (for example, a monolayer compared to a trilayer) as the general trend is that the reflectivity decreases with a decrease in the number of layers.

Fig. 7 shows the optical conductivity of bulk and 2D layered Mo_2CF_2. The optical conductivity is derived from $\varepsilon_2(\omega)$ and therefore displays a similar trend compared to the absorption and extinction coefficient spectra [Figs. 5(b) and 5(c)]. Optical conductivity peaks are observed around 0.76–2.41, 3.66–6.89 and 7.43–8.94 eV. The value of $\varepsilon_1(\omega)$ is negative [Fig. 4(a)] and the materials display anomalous dispersion [Fig. 4(b)] within
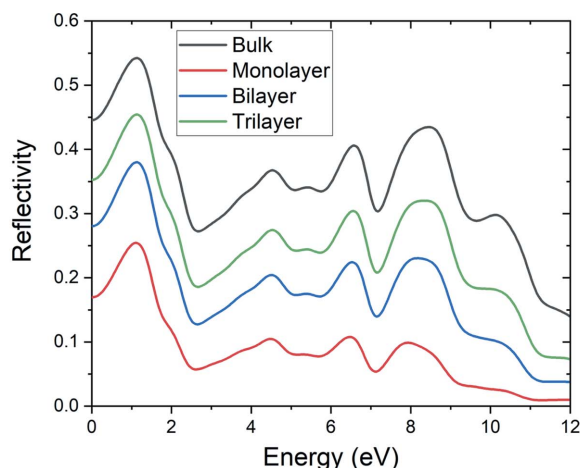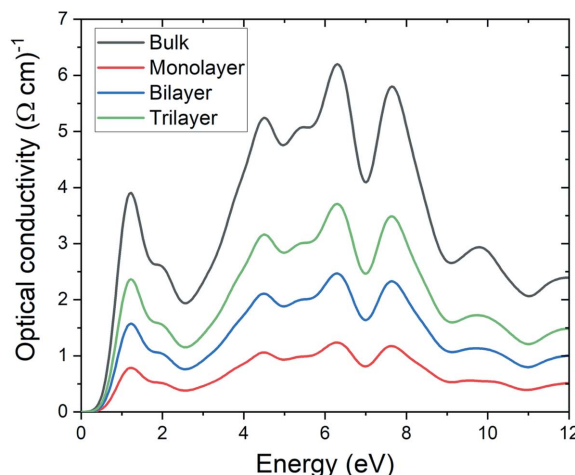

Figure 6
Reflectivity of bulk and 2D layered Mo_2CF_2.

Figure 7
Optical conductivity of bulk and 2D layered Mo_2CF_2.

these energy ranges, affirming the metallic behavior of Mo_2CF_2 at these energy ranges.

4. Conclusions

Using first principles density functional theory within the generalized gradient approximation (GGA) and the Perdew–Burke–Ernzerhof (PBE) functional, the electronic structure and optical properties of bulk and 2D layered (monolayer, bilayer and trilayer) Mo_2CF_2 were studied. The band gap energy of the 2D layered Mo_2CF_2 decreased as the number of layers increased due to interlayer coupling, which resulted in the splitting of the bands. Investigation of the optical properties of Mo_2CF_2 revealed that it behaves as a metal with an anomalous dispersion in the photon energy intervals of 0.68–2.19, 3.49–6.68 and 7.30–8.31 eV. Mo_2CF_2 also exhibited a high optical conductivity within these energy intervals. Regardless of the number of layers, Mo_2CF_2 was seen to be absorbing over a broad range of photon energies up to the vacuum ultraviolet region (greater than 6 eV photon energy or less than 200 nm wavelength), with a lower photon energy cut-off of 0.429 (2890), 0.387 (3204) and 0.345 (3594 nm) for the monolayer, bilayer and trilayer nanosheets, respectively, which is in the mid-infrared wavelength region. Its peak absorption range is in the vacuum ultraviolet region from about 6 to 11 eV (wavelengths of about 207 to 112 nm). A relatively low reflectivity is observed as the incident photon energy increases, particularly at photon energies between about 5 to 12 eV (about 248 to 103 nm). The band gap energy, static dielectric constant, optical dispersion, absorption, extinction coefficient, reflectivity, and conductivity of the 2D layered Mo_2CF_2 can be manipulated by controlling the number of layers. The unique behavior of its optical properties along with the ability to control its electronic and optical properties indicate the huge potential of 2D layered Mo_2CF_2 for various applications in the field of electronic devices.

References

Accelrys (2010). *Materials Studio CASTEP Manual.* Accelrys Inc., San Diego, California, USA. http://www.tcm.phy.cam.ac.uk/castep/documentation/WebHelp/CASTEP.html.

Anasori, B., Lukatskaya, M. R. & Gogotsi, Y. (2017). *Nat. Rev. Mater.* **2**, 16098.

Anasori, B., Xie, Y., Beidaghi, M., Lu, J., Hosler, B. C., Hultman, L., Kent, P. R. C., Gogotsi, Y. & Barsoum, M. W. (2015). *ACS Nano*, **9**, 9507–9516.

Bae, S., Kang, Y.-G., Khazaei, M., Ohno, K., Kim, Y.-H., Han, M. J., Chang, K. J. & Raebiger, H. (2021). *Mater. Today Adv.* **9**, 100118.

Cadatal-Raduban, M., Yoshikawa, A., Mui, L. V., Pham, M. H., Shimizu, T., Sarukura, N., Togashi, T. & Yamanoi, K. (2020). *Jpn J. Appl. Phys.* **59**, 052005.

Champagne, A., Shi, L., Ouisse, T., Hackens, B. & Charlier, J.-C. (2018). *Phys. Rev. B*, **97**, 115439.

Georgiou, T., Jalil, R., Belle, B. D., Britnell, L., Gorbachev, R. V., Morozov, S. V., Kim, Y. J., Gholinia, A., Haigh, S. J., Makarovsky, O., Eaves, L., Ponomarenko, L. A., Geim, A. K., Novoselov, K. S. & Mishchenko, A. (2012). *Nat. Nanotechnol.* **8**, 100–103.

Hong, L., Guo, R., Yuan, Y., Ji, X., Li, Z., Lin, Z. & Pan, W. (2020). *Mater. Today Energy*, **18**, 100521.

Hutchings, D. C., Sheik-Bahae, M., Hagan, D. J. & Van Stryland, E. W. (1992). *Opt. Quant. Electron.* **24**, 1–30.

Kaushik, P. D., Rodner, M., Lakshmi, G. B. V. S., Ivanov, I. G., Greczynski, G., Palisaitis, J., Eriksson, J., Solanki, P., Aziz, A., Siddiqui, A. M., Yakimova, R., Syväjärvi, M. & Yazdi, G. R. (2020). *Carbon*, **157**, 169–184.

Khan, S. A., Rehman, G., Ahmad, I., Maqbool, M., Franchini, C. & Amin, B. (2019). *Chem. Phys. Lett.* **731**, 136614.

Khazaei, M., Arai, M., Sasaki, T., Chung, C.-Y., Venkataramanan, N. S., Estili, M., Sakka, Y. & Kawazoe, Y. (2012). *Adv. Funct. Mater.* **23**, 2185–2192.

Khazaei, M., Arai, M., Sasaki, T., Estili, M. & Sakka, Y. (2014). *Phys. Chem. Chem. Phys.* **16**, 7841–7849.

Khazaei, M., Mishra, A., Venkataramanan, N. S., Singh, A. K. & Yunoki, S. (2019). *Curr. Opin. Solid State Mater. Sci.* **23**, 164–178.

Kramers, H. A. (1927). *Atti Congr. Int. Fis.* **2**, 545–557.

Kronig, R. de L. (1926). *J. Opt. Soc. Am.* **12**, 547–557.

Li, Z. & Wu, Y. (2019). *Small*, **15**, 1804736.

Mehta, V., Tankeshwar, K. & Saini, H. S. (2019). *AIP Conf. Proc.* **2115**, 030576.

Momma, K. & Izumi, F. (2011). *J. Appl. Cryst.* **44**, 1272–1276.

Mostafaei, A. & Abbasnejad, M. (2021). *J. Alloys Compd.* **857**, 157982.

Naguib, M., Kurtoglu, M., Presser, V., Lu, J., Niu, J., Heon, M., Hultman, L., Gogotsi, Y. & Barsoum, M. W. (2011). *Adv. Mater.* **23**, 4248–4253.

Naguib, M., Mochalin, V. N., Barsoum, M. W. & Gogotsi, Y. (2014). *Adv. Mater.* **26**, 992–1005.

Ostovari, F., Hasanpoori, M., Abbasnejad, M. & Salehi, M. A. (2018). *Physica B*, **541**, 6–13.

Peng, J., Chen, X., Ong, W.-J., Zhao, X. & Li, N. (2018). *Chem*, **5**, 18–50.

Qiu, B., Zhao, X., Hu, G., Yue, W., Ren, J. & Yuan, X. (2018). *Nanomaterials*, **8**, 962.

Segall, M. D., Lindan, P. J. D., Probert, M. J., Pickard, C. J., Hasnip, P. J., Clark, S. J. & Payne, M. C. (2002). *J. Phys. Condens. Matter*, **14**, 2717–2744.

Sinha, A., Dhanjai, Zhao, H., Huang, Y., Lu, X., Chen, J. & Jain, R. (2018). *TrAC Trends Anal. Chem.* **105**, 424–435.

Tamleh, S., Rezaei, G. & Jalilian, J. (2018). *Phys. Lett. A*, **382**, 339–345.

Wang, H., Wu, Y., Yuan, X., Zeng, G., Zhou, J., Wang, X. & Chew, J. W. (2018). *Adv. Mater.* **30**, 1704561.

Yorulmaz, U., Özden, A., Perkgöz, N. K., Ay, F. & Sevik, C. (2016). *Nanotechnology*, **27**, 335702.

Zhang, C. & Nicolosi, V. (2019). *Energy Storage Mater.* **16**, 102–125.

Zhu, J., Ha, E., Zhao, G., Zhou, Y., Huang, D., Yue, G., Hu, L., Sun, N., Wang, Y., Lee, L. Y. S., Xu, C., Wong, K. Y., Astruc, D. & Zhao, P. (2017). *Coord. Chem. Rev.* **352**, 306–327.